

# Dielectric metasurfaces for complete control of phase and polarization with subwavelength spatial resolution and high transmission

Amir Arbabi<sup>1</sup>, Yu Horie<sup>1</sup>, Mahmood Bagheri<sup>2</sup> and Andrei Faraon<sup>1\*</sup>

**Metasurfaces are planar structures that locally modify the polarization, phase and amplitude of light in reflection or transmission, thus enabling lithographically patterned flat optical components with functionalities controlled by design<sup>1,2</sup>. Transmissive metasurfaces are especially important, as most optical systems used in practice operate in transmission. Several types of transmissive metasurface have been realized<sup>3–6</sup>, but with either low transmission efficiencies or limited control over polarization and phase. Here, we show a metasurface platform based on high-contrast dielectric elliptical nanoposts that provides complete control of polarization and phase with subwavelength spatial resolution and an experimentally measured efficiency ranging from 72% to 97%, depending on the exact design. Such complete control enables the realization of most free-space transmissive optical elements such as lenses, phase plates, wave plates, polarizers, beamsplitters, as well as polarization-switchable phase holograms and arbitrary vector beam generators using the same metamaterial platform.**

Polarization, phase and amplitude completely characterize monochromatic light. In free-space optical systems, polarization is modified using wave retarders, polarizers and polarization beamsplitters, phase is shaped using lenses, curved mirrors or spatial phase modulators, and amplitude is controlled via neutral-density absorptive or reflective filters. Several metasurface platforms have been investigated recently to replicate the functionality of common optical components such as wave retarders, polarizers, beamsplitters, lenses or focusing mirrors. However, none of the platforms achieves complete control of both polarization and phase with subwavelength sampling and high transmission. A metasurface platform achieves complete control over polarization and phase if it can generate any desired physically admissible spatially varying polarization and phase distributions from an input beam with arbitrary polarization and phase distributions. Plasmonic metasurfaces have been demonstrated, but they have limited efficiencies because of fundamental limits<sup>7,8</sup> and metal absorption loss<sup>5,9,10</sup>. Components based on one-dimensional high-contrast gratings have higher efficiencies, but do not provide the high spatial resolution necessary for realizing precise phase or polarization profiles in the direction along the grating lines<sup>4,11–14</sup>. The majority of flat elements have been realized using a platform that provides only phase control<sup>3,4,6,11,13,15–20</sup> (in most cases only for a fixed input polarization) or only a limited polarization modification capability<sup>5,21–25</sup>. The platform we propose does not suffer from these limitations and provides a unified framework for realizing any device for polarization and phase control with an average transmission higher than 85%.

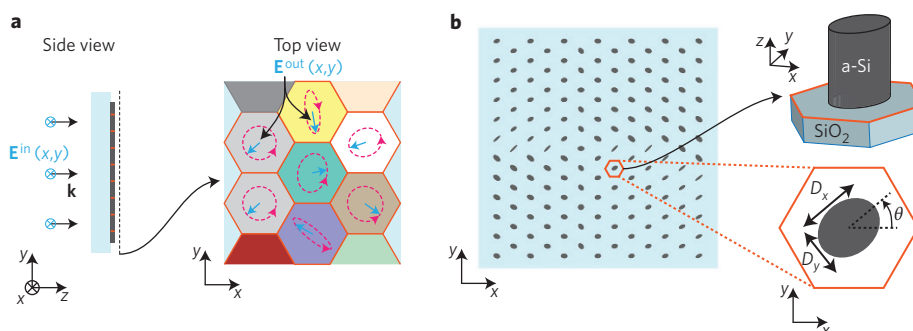
A generic illustration of a transmissive metasurface that provides spatially varying control of phase and polarization for monochromatic light is shown in Fig. 1a. In this illustration, the metasurface is divided into hexagonal pixels, but other lattice types could also be chosen. An optical wave with spatially varying electric field  $E^{\text{in}}$  is incident on the metasurface. The polarization ellipse and the phase of the optical field  $E^{\text{out}}$  transmitted through each pixel can be controlled arbitrarily by the pixel design (Fig. 1a, ‘Top view’). To avoid diffraction of light into non-zero diffraction orders and to achieve the high polarization and phase gradients required for implementation of optical components such as lenses with high numerical apertures, it is important that each pixel has a lateral dimension smaller than the wavelength. The general relation between the electric fields of the input and output waves at each pixel is expressed using the Jones matrix

$$T = \begin{bmatrix} T_{xx} & T_{xy} \\ T_{yx} & T_{yy} \end{bmatrix}$$

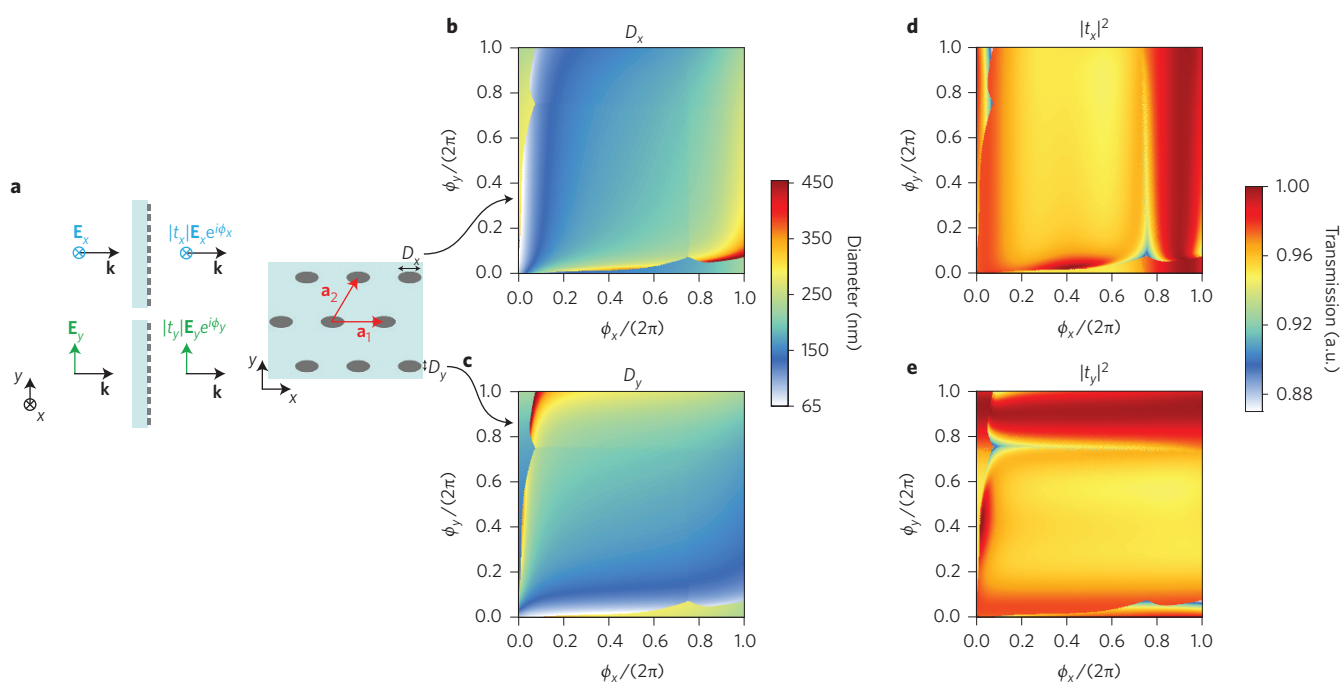
of the pixel as  $E^{\text{out}} = TE^{\text{in}}$ . It is shown in Supplementary Section 1 that, for metasurfaces with high transmission, any arbitrary ( $E^{\text{in}}$ ) can be mapped to any desired ( $E^{\text{out}}$ ) using a symmetric and unitary Jones matrix. Therefore, a metasurface platform achieves complete polarization and phase control if it can implement any unitary and symmetric Jones matrix at each pixel.

Figure 1b presents a schematic illustration of the proposed metasurface platform. This is composed of a single-layer array of amorphous silicon elliptical posts with different sizes and orientations, resting on a fused-silica substrate. The posts are placed at the centres of hexagonal unit cells. In a simplified picture, each post can be considered as a waveguide that is truncated on both sides and operates as a low-quality-factor Fabry–Pérot resonator. The elliptical cross-section of the waveguide leads to different effective refractive indices of the waveguide modes polarized along the two ellipse diameters. As a result, each of the posts imposes a polarization-dependent phase shift on the transmitted light and modifies both its phase and polarization. In the regime of operation considered here (also discussed previously in ref. 18), light is mainly confined inside the high-refractive-index posts, which behave as weakly coupled low-quality-factor resonators. Therefore, the light scattered by each post is primarily affected by the geometrical parameters of the post and has negligible dependence on the dimensions and orientations of its neighbouring posts. As a result, each unit cell of the lattice can be considered as a pixel, similar to the illustration shown in Fig. 1a.

<sup>1</sup>T.J. Watson Laboratory of Applied Physics, California Institute of Technology, 1200 E California Boulevard, Pasadena, California 91125, USA. <sup>2</sup>Jet Propulsion Laboratory, California Institute of Technology, Pasadena, California 91109, USA. \*e-mail: [faraon@caltech.edu](mailto:faraon@caltech.edu)



**Figure 1 | Illustration of the proposed metasurface for complete polarization and phase control.** **a**, Schematic side view (left) and top view (right) of a generic metasurface composed of hexagonal pixels. The polarization and phase of a normally incident optical wave with electric field  $\mathbf{E}^{\text{in}}(x,y)$  is modified at each pixel according to the pixel design. Pixels are coloured differently to emphasize that they can have different designs. In the top view, the spatially varying electric field of the output transmitted light ( $\mathbf{E}^{\text{out}}(x,y)$ ) at one moment in time and its polarization ellipse at each pixel are shown by blue arrows and red dashed ellipses, respectively. **b**, Top view of the proposed implementation of the metasurface. The metasurface is composed of elliptical amorphous silicon posts with the same height, but different diameters ( $D_x$  and  $D_y$ ) and orientations ( $\theta$ ). The posts are located at the centres of the hexagonal unit cells (pixels). Insets: schematic three-dimensional view of an amorphous silicon post and its magnified top view.



**Figure 2 | Birefringence of the elliptical post arrays.** **a**, Schematic illustration of a periodic array of elliptical posts with one of the ellipse axes aligned with one of the lattice vectors ( $\mathbf{a}_1$ ). The array exhibits an effective birefringence such that  $x$ - and  $y$ -polarized optical waves undergo different phase shifts as they transmit through the array. **b, c**, Simulated colour-coded values of the elliptical post diameters ( $D_x$  and  $D_y$ ) for achieving  $\phi_x$  and  $\phi_y$  phase shifts for  $x$ - and  $y$ -polarized optical waves, respectively. To realize a periodic array as shown in **a**, which imposes  $\phi_x$  and  $\phi_y$  phase shifts to  $x$ - and  $y$ -polarized optical waves, the diameter of the elliptical posts along  $x$  ( $D_x$ ) is obtained from **b**, and their corresponding diameter along  $y$  ( $D_y$ ) is found from **c**. **d, e**, Simulated colour-coded values of the intensity transmission coefficients corresponding to the choice of ellipse diameters shown in **b** and **c**.  $t_x$  and  $t_y$  represent amplitude transmission coefficients for  $x$ - and  $y$ -polarized light, respectively. An operating wavelength of 915 nm, lattice constant of 650 nm and amorphous silicon post height of 715 nm are assumed (see Methods for simulation details).

Light scattering by high-refractive-index single dielectric scatterers has been studied previously, and it has been shown that they may possess strong effective magnetic dipoles and exhibit large forward scattering<sup>26–28</sup> (Supplementary Fig. 1). Here, instead of studying the properties of a single elliptical post, we use a different approach and examine the transmission properties of periodic arrays of weakly coupled posts. Such periodic arrays better approximate the local transmission properties of a metasurface composed of gradually varying posts. We use the Jones matrix of the periodic array to approximate the local Jones matrix of each pixel. This

approximation is used here to successfully realize high-performance devices for polarization and phase control (discussed later in Figs 4 and 5), thus further validating its accuracy.

A periodic array of elliptical posts with one ellipse axis aligned to one of the hexagonal lattice vectors ( $\mathbf{a}_1$ , which is along the  $x$  axis) is shown in Fig. 2a. Due to symmetry, a normally incident optical wave linearly polarized along one of the ellipse axes does not change polarization and only acquires phase as it passes through the array. The phase shifts imposed by the array to the  $x$ - and  $y$ -polarized waves (that is,  $\phi_x$  and  $\phi_y$ ) are functions of the elliptical post

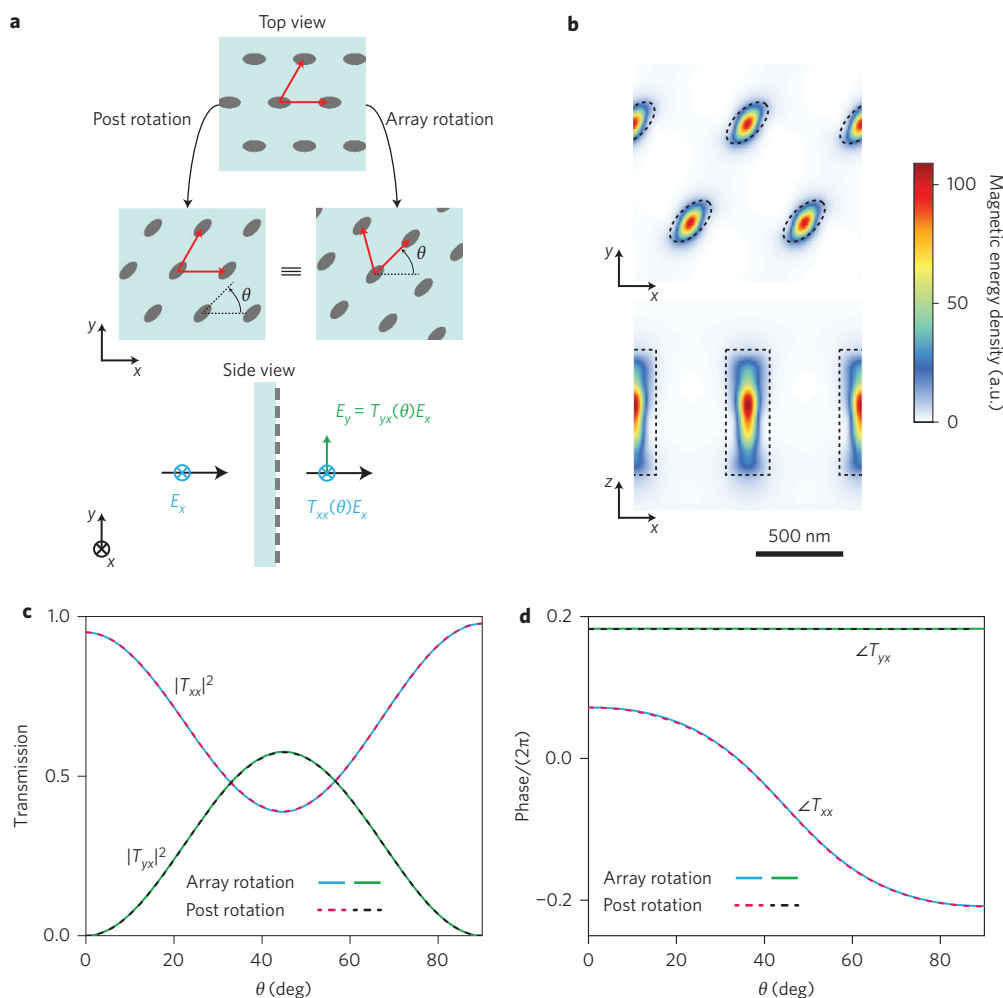


**Figure 3 | Equivalence of the array and post rotations.** **a**, Schematic illustrations of an array with one of the ellipse diameters aligned to one of the lattice vectors, and two arrays obtained from the first array either by only rotating the elliptical posts, or by rotating the entire array by the same angle  $\theta$ . Because of birefringence, the rotated arrays convert a portion of the incident  $x$ -polarized light to  $y$ -polarized light, as schematically illustrated in the side view. **b**, Simulated magnetic energy density when light propagates through an array of posts rotated by  $45^\circ$  with respect to the lattice. Dashed black lines depict the boundaries of the posts (top:  $x$ - $y$  cross-section; bottom:  $x$ - $z$  cross-section). **c,d**, Simulated values of two elements of the Jones matrices ( $T_{xx}$  and  $T_{yx}$ ) of the two arrays shown in **a**, as a function of  $\theta$ . The plots show that the coefficients are almost identical in both cases. See Methods for simulation details.

diameters  $D_x$  and  $D_y$ . Therefore, the array behaves as a two-dimensional material with adjustable birefringence whose principal axes are along the  $x$  and  $y$  directions. The phases ( $\phi_x$  and  $\phi_y$ ) and intensity transmission coefficients ( $|t_x|^2$  and  $|t_y|^2$ ) were first determined via simulations as functions of the ellipse diameters (see Methods and Supplementary Fig. 2 for details). From these simulations, the required diameters  $D_x$  and  $D_y$  to achieve all combinations of  $\phi_x$  and  $\phi_y$  while maintaining high transmission were derived and are plotted in Fig. 2b,c. Any combination of  $\phi_x$  and  $\phi_y$  can be simultaneously obtained by properly choosing  $D_x$  (from Fig. 2b) and  $D_y$  (from Fig. 2c). The corresponding intensity transmission coefficients ( $|t_x|^2$  and  $|t_y|^2$ ) are shown in Fig. 2d,e, and are larger than 87% for all values of  $\phi_x$  and  $\phi_y$ . The complete phase coverage combined with the high transmission results in the high performance of this platform.

The principal axes of the birefringent array shown in Fig. 2a can be rotated by rotating the entire array or, to a good approximation, by rotating all posts around their axes. This can be seen in Fig. 3, which shows that rotating the posts around their axes leads to approximately the same Jones matrix elements as rotating the entire array by the same angle. This is a result of the confinement of the optical energy inside the posts (as can be seen in Fig. 3b),

which has led to weak coupling among the posts<sup>18</sup>. This also provides further evidence that the polarization and phase transformation by the elliptical posts can be considered a local effect.

As we mentioned earlier, a metasurface can achieve complete polarization and phase control if each of its pixels can be designed to realize any unitary and symmetric Jones matrix. It is shown in Supplementary Section 2 that any desired symmetric and unitary Jones matrix can be realized using a birefringent metasurface if  $\phi_x$ ,  $\phi_y$ , and the angle between one of the principal axes of the material and the  $x$ -axis ( $\theta$ ) can be chosen freely. As Figs 2 and 3 show, all these degrees of freedom are achievable at each pixel through selection of the post diameters  $D_x$  and  $D_y$  and its in-plane rotation angle  $\theta$  (Fig. 1b, inset). Therefore, any desired spatially varying polarization and phase profiles can be generated by sampling the incident wavefront with a subwavelength lattice and placing elliptical posts with proper dimensions and rotation angles at the lattice sites to impart the required phase and polarization change on the transmitted light. The proposed metasurface platform samples both the incident and the transmitted wavefront with subwavelength resolution in both silica and air because the reciprocal vectors of the lattice are larger than the wavenumber of light and thus, for close to normal incidence, first-order diffraction is not present.

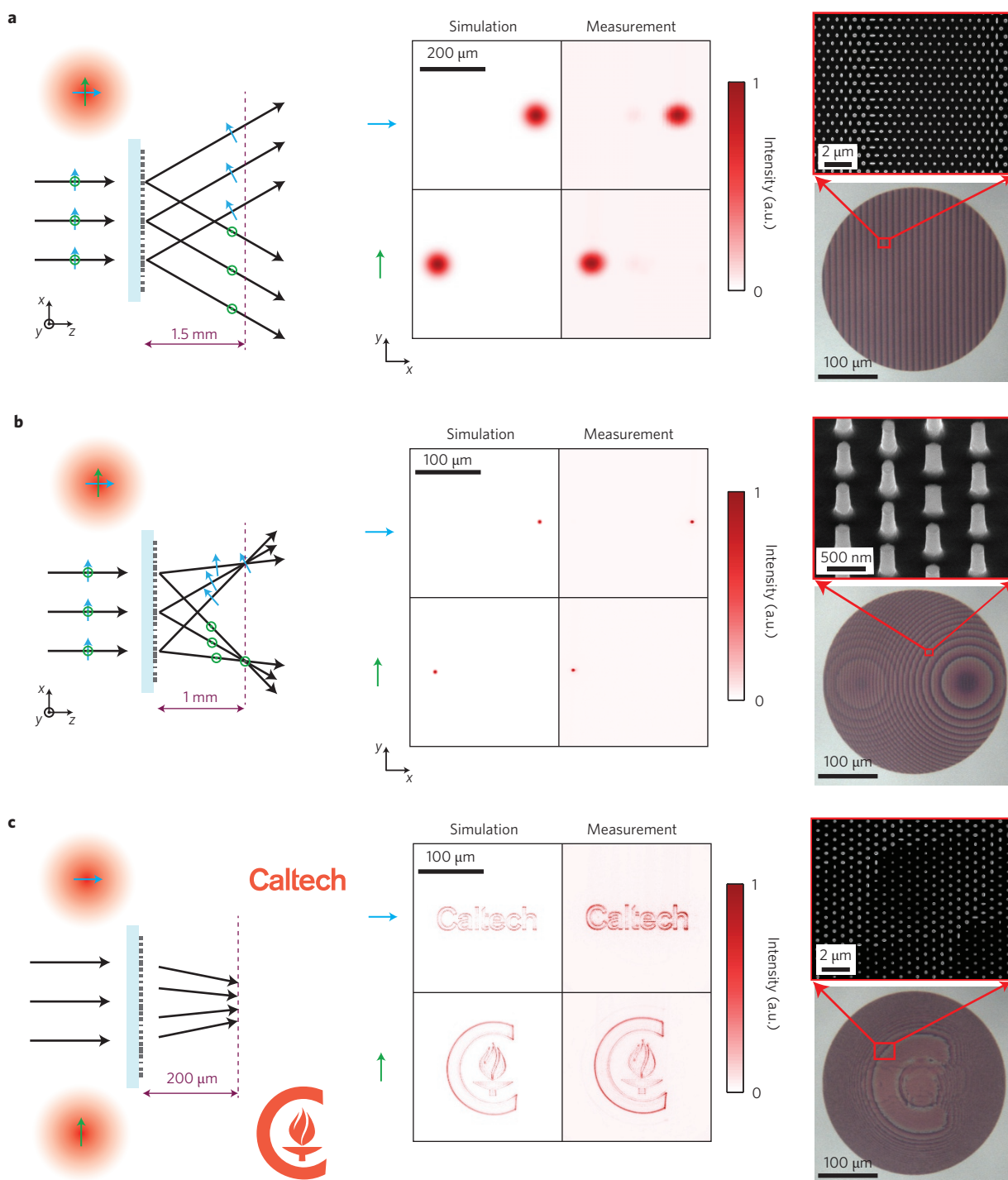


**Figure 4 | Devices for independent control of two polarizations.** **a**, A polarization beamsplitter that separates the x- and y-polarized light and deflects them by different angles ( $\pm 5^\circ$  in this case). The two angles can be chosen at will. **b**, A device that separates x- and y-polarized light and focuses them to two different points. The two different points can be chosen at will. **c**, A polarization-switchable phase hologram that generates two arbitrary patterns for x- and y-polarized light. In this case the word 'Caltech' is displayed for input x polarization and an icon is displayed for input y polarization. Left (**a-c**): schematic illustration of the devices. Middle (**a-c**): simulated and measured intensity profiles. Right (**a-c**): optical (bottom) and scanning electron (top) microscope images of the devices. Blue and green colours correspond to x and y incident polarizations, respectively.

The freedom provided by the proposed platform to simultaneously control the polarization and phase of light allows for implementation of a wide variety of optical components. To demonstrate the versatility and high performance of this platform, we fabricated and characterized two categories of flat optical elements operating at the near-infrared wavelength of 915 nm. The devices consist of 715 nm tall amorphous silicon posts with diameters

ranging from 65 to 455 nm, arranged on a hexagonal lattice with a lattice constant of 650 nm (for details of fabrication and measurement, see Methods). Devices belonging to the first category generate two different wavefronts for two orthogonal input polarizations. This functionality can be achieved if the device does not change the polarization ellipses of the two orthogonal polarizations it has been designed for and only changes their handedness



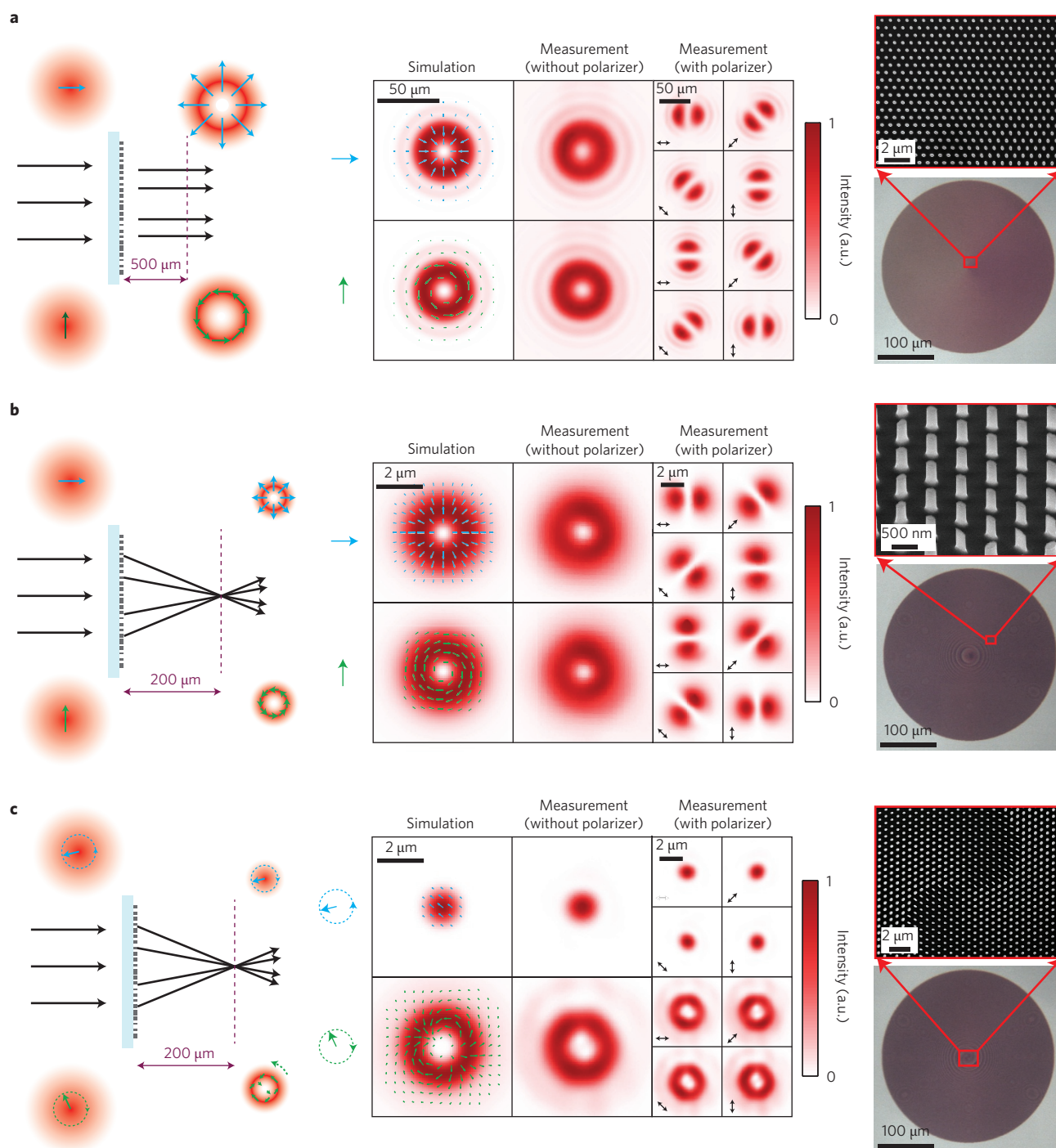


**Figure 5 | Devices for highly efficient vector beam generation.** **a**, Generation of radially and azimuthally polarized cylindrical vector beams from  $x$  and  $y$  linearly polarized beams. **b**, Simultaneous generation and focusing of radially and azimuthally polarized light from  $x$  and  $y$  linearly polarized beams. **c**, Device for focal spot control with incident polarization. Incident light is focused to a diffraction-limited spot or a doughnut-shaped spot depending on its helicity (right-hand or left-hand polarized). Left (**a–c**): schematic illustration of the devices. Middle (**a–c**): simulated and measured intensity profiles. Right (**a–c**): optical (bottom) and scanning electron (top) microscope images of the device. Measured intensity profiles are shown both with and without a linear polarizer placed in front of the camera. In **a** and **b**, blue and green colours correspond to  $x$  and  $y$  incident polarizations, respectively, and in **c** they correspond to right- and left-handed circularly polarized incident light, respectively. The black double-headed arrows show the direction of the polarizer's transmission axis.

(Supplementary Section 3). A special case occurs when both input polarizations are linear. Simulation and experimental measurement results, as well as optical and scanning electron microscope images of three types of device in this category, are shown in Fig. 4. A polarization beamsplitter that deflects  $x$ - and  $y$ -polarized portions of light by  $5^\circ$  and  $-5^\circ$  is presented in Fig. 4a. We measured 72% and 77%

efficiencies for the  $x$ - and  $y$ -polarized input light, respectively. The measured efficiencies are smaller than their corresponding simulated values (89% for  $x$ -polarized and 93% for  $y$ -polarized incident beams) because of slight differences between the diameters of the designed and fabricated posts. A polarization beamsplitter that separates and focuses the  $x$ - and  $y$ -polarized light to two different

points is presented in Fig. 4b. The focusing efficiency (defined as the ratio of the optical power focused to the desired spot to the input power) was measured as 80% and 83% for the  $x$ - and  $y$ -polarized light, respectively. A polarization-switchable phase hologram that generates two distinct patterns for  $x$ - and  $y$ -polarized light is shown in Fig. 4c. The change in the recorded pattern with polarization is shown in Supplementary Movie 1. This is the most general form of device from this category. We measured efficiencies of 84% and 91% for this device for  $x$ - and  $y$ -polarized incident light. The measured intensity profiles presented in Fig. 4 show the total transmitted light as detected by the camera, and there is no background subtraction.

Devices in the second category generate light with a desired arbitrary phase and polarization distribution from incident light with a given polarization. Figure 5a shows a device that transforms an incident  $x$ -polarized incident Gaussian beam into a radially polarized Bessel–Gauss beam, and a  $y$ -polarized incident Gaussian beam into an azimuthally polarized Bessel–Gauss beam. We measured transmission efficiencies of 96% and 97% for the  $x$  and  $y$  input polarizations, respectively. The measured intensity profiles for different polarization projections are also shown in Fig. 5. When the polarization of the incident Gaussian beam is linear but not aligned with the  $x$  or  $y$  axes, a generalized cylindrical vector beam is generated by this device. It has been shown recently that cylindrical vector beams show unique features such as focus shaping when focused with a high-numerical-aperture lens<sup>29</sup>. Furthermore, the same device in Fig. 5a generates light with different orbital angular momentum depending on the helicity of the input beam; right- and left-handed circularly polarized input beams will respectively acquire  $m = 1$  and  $m = -1$  units of orbital angular momentum as they pass through this device. Both the generation and focusing of cylindrical vector beams can be performed using a single device based on the proposed platform. Such a device, which simultaneously generates and focuses radially and azimuthally polarized light, is shown in Fig. 5b. Similar to the device shown in Fig. 5a, due to the polarization conversion, right- and left-handed polarized beams acquire plus or minus one units of orbital angular momentum as they pass through the device. As a result, by adding a sinusoidal dependence in the form of  $\exp(i\phi)$  to the phase profile of the device, the total orbital angular momentum of the right- and left-handed circularly polarized light after passing through the device will become  $m = 0$  and  $m = 2$ , respectively. A device with such a phase and polarization profile is shown in Fig. 5c. As can be seen from the simulation and measurement results, a right-handed circularly polarized incident beam is focused to a nearly diffraction-limited spot (Supplementary Fig. 3) while a left-handed circularly polarized beam is focused into a doughnut-shaped intensity pattern. Therefore, the focal spot shape can be modified by changing the polarization of the incident beam. This is particularly interesting because the polarization state of the incident beam can be switched rapidly using a phase modulator.

The functionalities provided by some of the optical devices demonstrated here can only be achieved by using a combination of multiple bulk optical components. For example, to realize the functionality of the polarization beamsplitter and focuser in Fig. 4b, a Wollaston prism and two carefully aligned lenses are required. The realization of the polarization vector beams shown in Fig. 5 generally requires interferometry<sup>30</sup>, liquid-crystal spatial light modulators, or conical Brewster prisms<sup>31</sup>. The complete and simultaneous control over the polarization and phase profiles of light offered by the proposed platform and the design technique enables the realization of novel optical components with functionalities exactly tailored to specific applications and with the form factors required for emerging applications such as wearable consumer electronics. As with most other diffractive optical elements, these devices have an optical bandwidth of several per cent of the

design wavelength<sup>32</sup>. Thus, they could directly replace conventional optics in applications employing narrow-band light sources such as optical communications, monochromatic imaging and multi-photon microscopy. We note that the theoretical approach and the design technique we introduce here are general and applicable to similar platforms with other types of scatterer and lattice shape, provided they offer complete and independent phase control for two orthogonal polarizations. The operating wavelength can also be changed by scaling the device dimensions. Further improvements are expected from using materials with optical nonlinearities and gain that might extend the spectral bandwidth of operation and provide tunability. These metasurfaces could also be patterned on curved or flexible substrates, thus enabling conformal optical devices.

## Methods

Methods and any associated references are available in the [online version of the paper](#).

Received 14 March 2015; accepted 20 July 2015;  
published online 31 August 2015

## References

- Kildishev, A. V., Boltasseva, A. & Shalae, V. M. Planar photonics with metasurfaces. *Science* **339**, 1232009 (2013).
- Yu, N. & Capasso, F. Flat optics with designer metasurfaces. *Nature Mater.* **13**, 139–150 (2014).
- Yu, N. *et al.* Light propagation with phase discontinuities: generalized laws of reflection and refraction. *Science* **334**, 333–337 (2011).
- Lin, D., Fan, P., Hasman, E. & Brongersma, M. L. Dielectric gradient metasurface optical elements. *Science* **345**, 298–302 (2014).
- Lin, J., Genevet, P., Kats, M. A., Antoniou, N. & Capasso, F. Nanostructured holograms for broadband manipulation of vector beams. *Nano Lett.* **13**, 4269–4274 (2013).
- Vo, S. *et al.* Sub-wavelength grating lenses with a twist. *IEEE Photon. Technol. Lett.* **26**, 1375–1378 (2014).
- Monticone, F., Estakhri, N. M. & Alù, A. Full control of nanoscale optical transmission with a composite metascreen. *Phys. Rev. Lett.* **110**, 203903 (2013).
- Arbabi, A. & Faraon, A. Fundamental limits of ultrathin metasurfaces. Preprint at <http://arXiv.org/abs/1411.2537> (2014).
- Aieta, F. *et al.* Aberration-free ultrathin flat lenses and axicons at telecom wavelengths based on plasmonic metasurfaces. *Nano Lett.* **12**, 4932–4936 (2012).
- Pfeiffer, C. & Grbic, A. Cascaded metasurfaces for complete phase and polarization control. *Appl. Phys. Lett.* **102**, 231116 (2013).
- Fattal, D., Li, J., Peng, Z., Fiorentino, M. & Beausoleil, R. G. Flat dielectric grating reflectors with focusing abilities. *Nature Photon.* **4**, 466–470 (2010).
- Lu, F., Sedgwick, F. G., Karagodsky, V., Chase, C. & Chang-Hasnain, C. J. Planar high-numerical-aperture low-loss focusing reflectors and lenses using subwavelength high contrast gratings. *Opt. Express* **18**, 12606–12614 (2010).
- Klemm, A. B. *et al.* Experimental high numerical aperture focusing with high contrast gratings. *Opt. Lett.* **38**, 3410–3413 (2013).
- Aieta, F., Kats, M. A., Genevet, P. & Capasso, F. Multiwavelength achromatic metasurfaces by dispersive phase compensation. *Science* **347**, 1342–1345 (2015).
- Warren, M., Smith, R., Vawter, G. & Wendt, J. High-efficiency subwavelength diffractive optical element in GaAs for 975 nm. *Opt. Lett.* **20**, 1441–1443 (1995).
- Lalanne, P., Astilean, S., Chavel, P., Cambil, E. & Launois, H. Design and fabrication of blazed binary diffractive elements with sampling periods smaller than the structural cutoff. *J. Opt. Soc. Am. A* **16**, 1143–1156 (1999).
- Arbabi, A. *et al.* Controlling the phase front of optical fiber beams using high contrast metastructures. *OSA Technical Digest, STu3M.4* (Optical Society of America, 2014).
- Arbabi, A., Horie, Y., Ball, A. J., Bagheri, M. & Faraon, A. Subwavelength-thick lenses with high numerical apertures and large efficiency based on high contrast transmittarrays. *Nature Commun.* **6**, 7069 (2015).
- West, P. R. *et al.* All-dielectric subwavelength metasurface focusing lens. *Opt. Express* **22**, 26212 (2014).
- Decker, M. *et al.* High-efficiency dielectric Huygens surfaces. *Adv. Opt. Mater.* **3**, 813–820 (2015).
- Kikuta, H., Ohira, Y. & Iwata, K. Achromatic quarter-wave plates using the dispersion of form birefringence. *Appl. Opt.* **36**, 1566–1572 (1997).
- Schonbrun, E., Seo, K. & Crozier, K. B. Reconfigurable imaging systems using elliptical nanowires. *Nano Lett.* **11**, 4299–4303 (2011).
- Yang, Y. *et al.* Dielectric meta-reflectarray for broadband linear polarization conversion and optical vortex generation. *Nano Lett.* **14**, 1394–1399 (2014).

24. Mutlu, M., Akosman, A. E., Kurt, G., Gokkavas, M. & Ozbay, E. Experimental realization of a high-contrast grating based broadband quarter-wave plate. *Opt. Express* **20**, 27966–27973 (2012).
25. Zhao, Y., Belkin, M. A. & Alù, A. Twisted optical metamaterials for planarized ultrathin broadband circular polarizers. *Nature Commun.* **3**, 870 (2012).
26. García-Etxarri, A. *et al.* Strong magnetic response of submicron silicon particles in the infrared. *Opt. Express* **19**, 4815–4826 (2011).
27. Evlyukhin, A. B., Reinhardt, C. & Chichkov, B. N. Multipole light scattering by nonspherical nanoparticles in the discrete dipole approximation. *Phys. Rev. B* **84**, 235429 (2011).
28. Spinelli, P., Verschuuren, M. A. & Polman, A. Broadband omnidirectional antireflection coating based on subwavelength surface Mie resonators. *Nature Commun.* **3**, 692 (2012).
29. Zhan, Q. Cylindrical vector beams: from mathematical concepts to applications. *Adv. Opt. Photon.* **1**, 1–57 (2009).
30. Phelan, C. F., Donegan, J. F. & Lunney, J. G. Generation of a radially polarized light beam using internal conical diffraction. *Opt. Express* **19**, 21793–21802 (2011).
31. Kozawa, Y. & Sato, S. Generation of a radially polarized laser beam by use of a conical Brewster prism. *Opt. Lett.* **30**, 3063 (2005).
32. Swanson, G. J. Binary optics technology: the theory and design of multi-level diffractive optical elements. Technical Report 845 (Massachusetts Institute of Technology, DTIC, 1989).

## Acknowledgements

This work was supported by the Caltech/JPL President and Director Fund (PDF) and the Defense Advanced Research Projects Agency (DARPA). Y.H. was supported as part of the Department of Energy (DOE) 'Light-Material Interactions in Energy Conversion' Energy Frontier Research Centre under grant no. DE-SC0001293 and a Japan Student Services Organization (JASSO) fellowship. Device nanofabrication was performed at the Kavli Nanoscience Institute at Caltech. The authors thank D. Fattal and C. Santori for discussions.

## Author contributions

A.A. and A.F. conceived the experiment. A.A., Y.H. and M.B. fabricated the samples. A.A. performed the simulations, measurements and analysed the data. A.A. and A.F. co-wrote the manuscript. All authors discussed the results and commented on the manuscript.

## Additional information

Supplementary information is available in the [online version](#) of the paper. Reprints and permissions information is available online at [www.nature.com/reprints](http://www.nature.com/reprints). Correspondence and requests for materials should be addressed to A.F.

## Competing financial interests

The authors declare no competing financial interests.



## Methods

**Simulations and design.** To obtain the simulation results presented in Fig. 2b,c, we computed the transmission coefficients  $t_x$  and  $t_y$  of  $x$ - and  $y$ -polarized plane waves for the periodic array shown schematically in Fig. 2a by using the rigorous coupled wave analysis (RCWA) technique using a freely available software package<sup>33</sup>. The simulations were performed at  $\lambda = 915$  nm. The amorphous silicon posts (refractive index of 3.56 at 915 nm) are 715 nm tall and rest on a fused-silica substrate. We computed these transmission coefficients for all mutual values of the ellipse diameters  $D_x$  and  $D_y$  in the range  $0.1a$ – $0.7a$ , where  $a = 650$  nm is the lattice constant. Simulation results are presented in Supplementary Fig. 2. For normal incidence, the array is non-diffractive in both air and fused silica at wavelengths longer than  $\lambda_1 = n_{\text{SiO}_2} \sqrt{3}/2a = 816$  nm. Next, using the computed transmission coefficients for all combinations of phases  $\phi_x$  and  $\phi_y$ , we found the diameters  $D_x$  and  $D_y$  that minimize the mean squared error  $E = 1/2(|t_x - e^{i\phi_x}|^2 + |t_y - e^{i\phi_y}|^2)$ . It should be noted that the elliptical posts obtained using this method do not possess resonances close to the operation wavelength because the transmission values go to zero at resonance and increase the mean squared error. Transmission spectra for a few arrays with different diameters are presented in Supplementary Fig. 4.

The simulation results presented in Fig. 3b–d were also computed using the RCWA technique. In Fig. 3b,  $x$ -polarized light with magnetic energy density of 1 is normally incident on the posts from the top. The simulation parameters used to obtain Fig. 3b–d are the same as the ones used in Fig. 2, and the diameters of the elliptical posts are 300 and 150 nm.

To design the devices presented in Fig. 4, which impose two distinct phase profiles to  $x$ - and  $y$ -polarized light, the optimum phase profiles that generate the desired patterns were first determined by back-propagating the desired pattern to the plane of the device and finding the phase difference between the back-propagated wave and the incident wave. This method is discussed in details in ref. 18. After finding the desired phase profiles for both polarizations, the profiles were sampled at the lattice sites, and elliptical posts with major and minor diameters that would impart the required phases to the transmitted beam were placed on those sites.

The optical elements shown in Fig. 5 that simultaneously modify the polarization and phase of the light were designed to generate a desired spatially varying optical wave from a given input optical wave profile. We first sampled the input and output optical waves at the lattice sites, then computed the Jones matrix and decomposed it into its eigenvalues and eigenvectors to determine the desired phase shifts for waves polarized along the axes of the ellipse (that is,  $\phi_x$  and  $\phi_y$ ) and the rotation angle  $\theta$  (for details see Supplementary Sections 1 and 2). Finally, from Fig. 2b,c we found the diameters of the elliptical posts imposing the target  $\phi_x$  and  $\phi_y$  phase shifts, rotated them anticlockwise by their  $\theta$ , and placed them at their corresponding lattice sites.

The simulation results presented in Figs 4 and 5 were computed by assuming that the devices perform the polarization and phase conversions ideally and with  $\lambda/15$  spatial resolution. For these simulations, the input light was assumed to be in the form of uniformly polarized Gaussian beams with the same beam radius as the illumination beam radius used in the corresponding measurements (35  $\mu\text{m}$  for the device shown in Fig. 4a and 80  $\mu\text{m}$  for the devices shown in Figs 4b,c and 5). The output light was computed at each point on a rectangular grid assuming ideal polarization and phase conversion by the device and then propagated to the planes of interest using the plane wave expansion technique<sup>34</sup>.

**Sample fabrication.** The devices shown in Figs 4 and 5 were fabricated on a fused-silica substrate. A layer of 715 nm hydrogenated amorphous silicon was deposited using plasma-enhanced chemical vapour deposition (PECVD) with a 5% mixture of silane in argon at 200 °C. Positive electron beam resist (300 nm, ZEP-520A) was then spin-coated, as well as  $\sim 60$  nm of a water-soluble anti-charging conductive polymer (aquaSave, Mitsubishi Rayon) to avoid static charging during electron-beam lithography. The pattern was written on the resist using electron-beam lithography, the anti-charging layer was removed in water, and the pattern was

developed in a resist developer (ZED-N50, Zeon Chemicals). A 70-nm-thick aluminium oxide layer was then deposited on the developed resist and patterned by lifting off the resist. The patterned aluminium oxide was subsequently used as a hard mask for dry etching of amorphous silicon in a 3:1 mixture of  $\text{SF}_6$  and  $\text{C}_4\text{F}_8$ . Finally, the aluminium oxide mask was removed using a 1:1 mixture of ammonium hydroxide and hydrogen peroxide heated to 80 °C.

To compensate for systematic fabrication errors such as a non-optimum exposure dose in the electron-beam lithography patterning and possible undercutting during dry etching, for each of the devices shown in Figs 4 and 5 we fabricated a series of devices with all post diameters uniformly biased from their optimum design values in steps of 5 nm. Characterization results for the devices with different diameters showed that the device functionalities were not severely affected by these intentionally introduced systematic errors; only the device efficiencies were reduced from their maximum values by  $\sim 3\%$  per each 5 nm error in the post diameters.

**Measurement procedure.** The devices were characterized using the set-up shown schematically in Supplementary Fig. 5a. Light from a 915 nm fibre-coupled semiconductor laser was passed through a fibre polarization controller and collimated to generate a Gaussian beam. To collimate the fibre output and generate Gaussian beams with a beam radius smaller than the device radius, we used a fibre collimation package (Thorlabs F220APC-780) and a lens (Thorlabs LB1676-B with focal length of 10 cm to measure the devices in Fig. 4a and Thorlabs LB1945-B with a focal length of 20 cm for the devices shown in Figs 4b,c and 5). The illumination beam radius on the sample was adjusted by changing the distance between the lens and the sample. The beam radius was set to  $\sim 35$   $\mu\text{m}$  to measure the device shown in Fig. 4a to avoid overlap of the deflected and non-deflected portions of the output light at the measurement plane. To fill most of the device physical aperture, the illumination beam radius was set to 80  $\mu\text{m}$  for all other measurements reported in Figs 4b,c and 5. The objective lens, the tube lens (Thorlabs LB1945-B) and the camera (CoolSNAP K4, Photometrics) shown in Supplementary Fig. 5a comprise a custom-built microscope. We used three different objective lenses to achieve different magnifications. The measurement results shown in Fig. 4a were obtained using a  $\times 20$  objective lens (Olympus UMPlanFI, NA = 0.4), the results shown in Figs 4b,c and 5a were recorded using a  $\times 50$  objective lens (Olympus LCPlan N, NA = 0.65) and those presented in Fig. 5b,c were obtained using a  $\times 100$  objective lens (Olympus UMPlanFI, NA = 0.95). The overall microscope magnification for each objective lens was found by imaging a calibration sample with known feature sizes. The polarizer (Thorlabs LPNIR050-MP) was inserted into the set-up to confirm the polarization state of the incident light (after removing the device) and the output light. Efficiency values for the devices shown in Figs 4a,c and 5 were obtained by integrating the light intensity on the camera (that is, the measured intensity profiles shown in Figs 4 and 5), subtracting the dark noise, and normalizing it to the integrated intensity recorded when the device was removed. For the device shown in Fig. 4a, only the intensity of the deflected portion of the output light was used for efficiency calculation. To characterize the efficiency of the device shown in Fig. 4b we used the set-up shown schematically in Supplementary Fig. 5b. A 25- $\mu\text{m}$ -diameter pinhole (Thorlabs P25S) was placed at the focal plane of the device and was aligned such that only the light focused to one of the two focal points could pass through it. To obtain the reported efficiencies, the optical power passed through the pinhole was measured using a power meter (Thorlabs PM100D with Thorlabs S122C power sensor) and was divided by the power of the incident beam, which was measured before the device.

## References

33. Liu, V. & Fan, S. S4: a free electromagnetic solver for layered periodic structures. *Comput. Phys. Commun.* **183**, 2233–2244 (2012).
34. Born, M. & Wolf, E. *Principles of Optics* (Cambridge Univ. Press, 1999).